sustainability

MDPI

Article

Dual-Level Voltage Bipolar Thermal Energy Harvesting System from Solar Radiation in Malaysia

Muhammad Nazri Rejab [1,*], Omar Mohd Faizan Marwah [1,*], Muhammad Akmal Johar [2] and Mohamed Najib Ribuan [3]

[1] Faculty of Mechanical and Manufacturing Engineering, Tun Hussein Onn University, Parit Raja 86400, Malaysia
[2] Technical Delivery Excellence, Level 21, PETRONAS Tower 3, Persiaran KLCC, Kuala Lumpur City Centre, Kuala Lumpur 50088, Malaysia
[3] Faculty of Electric and Electronic Engineering, Tun Hussein Onn University, Parit Raja 86400, Malaysia
* Correspondence: mnr190020@gmail.com (M.N.R.); mdfaizan@uthm.edu.my (O.M.F.M.)

Abstract: Harvesting energy from solar radiation in Malaysia attracts the attention of researchers to utilize the potential by ongoing improvement. Roofing material with low albedo absorbs the heat, that can then be harvested using a thermoelectric generator. Previous research only measured the open-circuit voltage with different thermoelectric generator configurations. Low power output limits the potential to be utilized. The low output power can be increased using a DC converter. However, the converter must be tuned concerning low- and high-voltage levels, bipolar, and the maximum power point tracking. Therefore, this paper presents a dual-level voltage bipolar (DLVB) thermal energy harvesting system. The circuit is tested at constant and various time intervals to evaluate the system's functionality and performance. Experiment results show that the proposed harvesting system can boost from 0.6 and 1.6 V to achieve the optimum level. The mean efficiency of the harvesting circuit obtains 91.92% at various time intervals. Further, the field test result obtains output power from 1.45 to 66.1 mW, with the mean efficiency range of 89.62% to 92.98%. Furthermore, recommendations are listed for future research.

Keywords: thermoelectric generator; bipolar; dual-level; real-time; solar radiation; low temperature

Citation: Rejab, M.N.; Marwah, O.M.F.; Johar, M.A.; Ribuan, M.N. Dual-Level Voltage Bipolar Thermal Energy Harvesting System from Solar Radiation in Malaysia. *Sustainability* **2022**, *14*, 12521. https://doi.org/10.3390/su141912521

Academic Editors: Erol Kurt and Jose Manuel Lopez-Guede

Received: 15 August 2022
Accepted: 8 September 2022
Published: 30 September 2022

Publisher's Note: MDPI stays neutral with regard to jurisdictional claims in published maps and institutional affiliations.

1. Introduction

Recently, energy harvesting has become the main focus of research to provide power for devices, with various design approaches and methods for energy conversion [1–4]. Solar energy is one renewable energy (RE) that is gaining attention for implementation in Malaysia [2]. In addition, the increase in solar power plants proves the vast amount of solar radiation available to be utilized at the optimum level. Several policies and incentives were introduced in 2016 by the Energy Commission in Renewable Energy Act 2011, which paved the way for the Feed-in Tariff (FiT) system and net energy metering (NEM) [3]. Commonly, solar energy is utilized from heat or light to convert it into electrical energy [4]. Perhaps the most popular is electrical energy, which employs solar cells. Solar energy research focuses on designing and implementing photovoltaic (PV) technologies in contrast to solar thermal technologies. Practically, solar energy is recognized as an alternative energy source for power generation and thermal applications. However, utilizing solar thermal energy requires detailed design evaluation to increase the conversion efficiency [3,5,6].

The solar thermoelectric generator (STEG), which converts solar radiation heat into electrical energy using a thermoelectric generator (TEG), has gained researchers' attention. The STEG needs additional components, such as the optical collector, thermal storage, TEG, vacuum encapsulation, and heat sink [7]. In addition, the Fresnel lens and concentrator are also used to increase the solar concentration of the TEG. However, it makes the system bulky, concerning the roof-mount for domestic implementation. Furthermore, research

has been conducted on improving the performance in different ways [8,9]. Some of these methods, for instance, include using PCMs [10], nano-enhanced PCMs [11–13], thermoelectric cooler [14], TEGs [15], nanofluids [16–18], nano-enhanced coatings [19], electrical heaters [20], and a solar collector [21]. Table 1 summarizes TEG's integration in the hybrid system to harvest thermal energy. The methods used mainly depend on the specific design of the solar system and the possibilities observed for performance enhancement or taking advantage of the further availability in the system to generate other types of energy. TEGs tend to improve the efficiency of the hybrid system at low-temperature values, but most of the power generated is from the PV. The emergence of TEG material technology to improve the figure of merit, ZT, will help to increase the TEG's performance to harvest thermal energy. The TEG must be separate from the hybrid system to evaluate the TEG's performance of harvesting thermal energy from solar radiation [22]. Therefore, the capability of the TEG in a simple experiment and field setup is conducted through this research, focusing on roofing materials.

Table 1. The comparison of different solar thermal implementation.

Types	Description	Remark	Conclusion
CPV-TEG	- Using TEG, CPV, and nanofluid cooling block (NCPV-T) to compare with sole PV, CPV-TEG with metal heatsink, and CPV-TEG with nano. Evaluate the absorbed thermal energy by the coolant as the output [23].	- The result indicates that without a suitable heat exchanger, the TEG negatively affects the overall CPV system.	- However, the perspective of both systems' reaction to a particular application makes it difficult and complex to unquestionably determine whether the hybridization is generally beneficial or not. - Nevertheless, the integration of TEG with CPV indicates the potential and advantages, but in the end, is a better comparison with other potential hybrid systems to understand the significant advantages of these systems. - TEG attached on the rear side of the PV negatively affects CPV compared to unconcentrated PV, no matter how efficient the heat exchanger at the cold side.
	- Investigated the performance of hybrid CPV-TEG via a thermal resistance model [24].	- The CPV-TEG output power is 1.24–2.85% higher than sole CPV. However, the operating temperature of CPV-TEG is higher.	
	- Proposed a parabolic trough reflector with a sun-tracking system and a receiver on its concentration axis [25].	- The system's daily average efficiency was 57.52% lower than the standalone PV. In addition, obtained a higher temperature of the PV cell (94 °C) than the standalone PV cell (52 °C).	
	- Proposed a TEG to a CPV thermal (CPVT) system consisting of a parabolic trough concentrator with a hybrid receiver (PV-TEG) system [26].	- The efficiency improved by 7.46%, and the output power was compared to the CPVT without a TEG. However, the operating temperature of the PV cell increased from 56 °C in the CPVT system to 63 °C in the proposed system.	
Techniques to bypass the negative effects of TEG on PV	- The use of the optical concentrator, PV, TEG, and two cooling cycles in the CPV-T-TEG system to overcome the disadvantages of the conventional hybrid systems [27].	- The proposed system obtains a higher output power than CPV and slightly lower than CPV-TEG. Moreover, TEG contributes more than 8% to the overall output, with a 10% increase in cost per output power compared to the conventional system.	- The drawback of the method is a reduction of the PV performance and lifetime due to the high operating temperature.

Table 1. *Cont.*

Types	Description	Remark	Conclusion
PV-TEG with thermal concentration	- The thermal concentrator used a flat-plate micro-channel heat pipe (MCHP) [28].	- An extra cost is needed for hybridization compared to sole PV.	- The thermal resistance will increase when a heat exchanger or a conducting plate is applied between the PV and TEG.
	- Conducted preliminary experiments on a hybrid PV-MCHP- TEG system compared with sole PV [29].	- The temperature of PV is higher (~50 °C) than sole PV (~40 °C), with a temperature difference of 10 °C at the TEG.	- Affect the amount of heat at TEG (hot side) and cooling load on PV.
	- Proposed a hybrid PV-MCHP-TEG system by adding a water-cooling block to the cold side of the TEG [30].	- The PV temperature obtains 62 °C, slightly lower than sole PV.	- The thermal concentration caused the increase of PV temperature and the temperature gradient. Thus, degradation of the performance of PV in long-term operation.
	- TEG modules attach to a copper plate at the rear PV. A water-cooling block is used as a heat sink [31].	- The maximum temperature of PV and temperature difference at TEG are 80 °C and 52 °C, respectively.	
Unconcentrated PV-TEG system	- The thermal contact resistance between the TEG and heat sink is the most influential on the system's performance [32].	- Neglected all the contact resistances, causing overestimation of the output power and efficiency of the hybrid system.	- The contribution of the TEG should be distinguished from the hybrid system to have a clear view due to the cooling effect provided by a heat exchanger.
	- The temperature gradient is difficult to maintain considerably across the TEG [33].	- The TEG improved by 4.5% for the maximum efficiency.	
	- Obtained an 8–43 °C temperature gradient across the TEG [34].	- The system efficiency is approximately equal to sole PV under standard conditions.	
	- The heat exchanger implements a water block with different solutions of cobalt oxide and the addition of phase change materials [35].	-The temperature difference across the TEG reaches approximately 10 °C.	
	- The TEG is mounted to the rear side of PV, and the TEG cold side temperature is constant at 20 °C [36].	- The output energy increase was 5%, with a 6% increase in the overall efficiency obtained compared to a sole PV.	
	- The TEG is directly attached to the rear side of a PV, and the TEG cold side was exposed to the ambient temperature [37].	- The PV efficiency improves at 0.59% and the output power at 5.06%. The maximum temperature difference at TEG is 2.48 °C.	
	- The TEG heat exchanger employed PCM [38].	- The PV-TEG-PCM system obtained 9.5% power enhancement. It is observed that the system performs better when the cooling source is from the natural convection.	

Fewer studies on the application of solar thermal technologies have been carried out in Malaysia, as solar thermal is still an emerging technology compared to PV technology. Therefore, Malaysia has a promising development for solar energy due to its tropical climatic conditions, which give abundant sunlight and high irradiance levels, with a solar radiation level from 4.21 to 5.56 kWh/m^2 [39]. From Malaysia's perspective, the research

related to thermal energy harvesting (TEH) from solar thermal energy is summarized in Table 2.

Table 2. The summary of thermal energy harvesting from solar thermal energy.

Application	Temperature Difference, °C	Output	Thermal Energy Harvesting System	Year	References
Asphalt (Field)	23	1.02 V	BQ25505	2021	[40]
Asphalt (Field)	7.95	5.3 V	ECT 310	2020	[41]
PV-TEG (Experimental)	8	0.5–3 mW based on Voc	No	2019	[42]
PV-TEG (Numerical)	56.1	119 W	No	2019	[43]
Asphalt (Experimental)	2.49	5.6 µW based on Voc	No	2019	[44]
Asphalt (Experimental)	29.77	2.39 V Voc	No	2019	[45]
Shingle (Experimental)	3	65.22 µW based on Voc	No	2017	[46]
Solar pond (Simulation)	40 to 100	8 W	No	2017	[47]
PV-TEG (Experimental)	10 to 40	0.3 to 1.35 V Voc	No	2012	[48]

Based on Table 2, the research on thermal harvesting in Malaysia only measures the open-circuit voltage, Voc, of TEG due to solar radiation. Recently, two studies have implemented the thermal energy harvesting system (TEHS) to evaluate the potential of the TEG. However, the TEHS used is only suitable for unipolar conditions.

On the other hand, the houses are exposed to sizeable radiant heat gains on roofs due to higher solar altitudes during the daytime [49], with the hottest time being from 11.30 a.m. to 4.30 p.m. [42]. Heat gain from the roof contributed 70% of total heat gain in tropical houses [49,50]. Moreover, the building is directly exposed to solar radiation-stored thermal energy, especially on the roof, due to the low albedo characteristic of the roof material [42,51].

In further research [52], the temperature difference in a building was obtained as 1.6 to 1.9 °C from 1.00 p.m. until 5.00 p.m. A field study by Toe and Kubota [53] on a two-story modern terrace house in Malaysia demonstrates that the surface temperature of the ceiling beneath the roof recorded the highest value during the daytime, which was 2.7 °C higher than the room air temperature. Besides daytime, the temperature difference is also available at night [54]. Therefore, it should be evaluated for potential thermal energy.

Furthermore, most residential buildings' roofs are under substantial solar radiation during the day, resulting in as high as 60 °C in the attics compared to the conditioned living space underneath [55]. Therefore, harvested thermal energy from the roof and attic areas can be evaluated. The authors of [56] emphasized that research must be conducted to assess the feasibility and viability of solar thermal energy at low temperatures. The author of [46] evaluated the potential of TEGs on shingle, focusing on the effect of solar radiation on temperature differences. The result indicates that the output power is 65.22 µW at 138 Ω from the experiment, with a temperature difference at a TEG of 3 °C. However, the research only measured the open-circuit voltage of the TEG. The author emphasized the development of a thermal energy harvesting system. Therefore, further research must evaluate the full potential of thermal energy harvesting integrated with the storage system.

The TEG is a maintenance-free semiconductor device suitable for converting thermal energy from solar radiation into electrical energy by establishing a temperature difference across thermoelectric devices. The TEG converts thermal energy to electrical energy via the principle of Seebeck [57]. The generated power depends heavily on the temperature differ-

ence, which will inevitably fluctuate, especially in real-time applications. A disadvantage of this energy conversion method is its efficiency. The efficiency of the thermoelectric module as an energy converter is low [4]. However, a TEG has a high power density among various energy sources [58]. Still, the polarity of the TEG voltage output is unpredictable since the temperature difference between the hot and cold sides of the TEG is reversible in real-time implementation [59–61]. Therefore, it is compulsory to design and develop a bipolar circuit system to be practically used in real-time thermal energy harvesting. However, the bipolar-input harvester is more complicated than the conventional harvesting circuit [62]. In addition, the output voltage from the TEG is too low to power up these devices. Thus, a DC converter is essential to increase the low-voltage input to the high-voltage output. For specific power supply scenarios, additional components could be selectively configured.

A DC-to-DC boost converter can boost the output voltage of the TEG to an appropriate higher level, and an energy storage unit such as a battery or capacitor can be loaded for emergencies. A maximum power point tracking (MPPT) can draw the maximum available output power of the TEG by matching its input impedance with that of the source [57,63]. The authors of [58] proposed a DC boost converter with bipolar-input bipolar-output, with maximum power point tracking (MPPT), zero-crossing switching (ZCS), and a control logic circuit. However, the converter operated in discontinuous mode (DCM) at a constant voltage level. In [62], the bipolar circuit integrated with a boost/flyback hybrid converter and maximum power point tracking (MPPT) at a low-voltage level is proposed at a constant voltage. On the other hand, the input TEG voltage level is an additional factor to consider [59]. The input TEG voltage is proportional to the TEG array configuration and the temperature gradient.

Therefore, designing the thermal energy harvesting circuit from solar radiation in real-time implementation should consider the electrical bipolarity, the low and high input voltage from TEG, the DC boost converter, the TEG array configuration, and the rapid temperature fluctuation. Thus, this research work describes the development of a thermal energy harvesting circuit that considers all the factors integrated with MPPT to obtain optimum power transfer for real-time implementation. In detail, the novelty and contributions of this research work are in designing the dual-level voltage bipolar (DLVB) harvesting system to harvest thermal energy due to solar radiation in Malaysia. In addition, the system is integrated with the MPPT algorithm and DC boost converter to improve its performance.

The thermoelectric generator is described in Section 2, followed by the method and instruments of the preliminary work for real-time data, explained in Section 3. Then, Section 4 briefly describes the details of the design and development of the thermal energy harvesting system structure and the system's topology in this research work. The result of the harvesting circuit is presented in Section 5. Next, the results are discussed in Section 6. Finally, the conclusion and recommendations for future work are presented in Sections 7 and 8, respectively.

2. Thermoelectric Generator

A thermoelectric generator consists of p-type and n-type semiconductors connected electrically in series and thermally in parallel. Figure 1 shows the 1D schematic of a TEG along with the heat source (Q_H), heat dispersed (Q_C), internal resistance (R_{TEG}), and hot side (T_H) and cold side (T_C) temperature.

The heat balance at the hot side is described as Equation (1), and at the cold side as Equation (2):

$$Q_H = \alpha T_H I + \left(\frac{\lambda A}{L}\right)\Delta T - 0.5 I^2 R_{TEG} \quad (1)$$

$$Q_C = \alpha T_C I + \left(\frac{\lambda A}{L}\right)\Delta T - 0.5 I^2 R_{TEG} \quad (2)$$

where α is the Seebeck coefficient, T_H is the hot side temperature, T_C is the cold side temperature, λ is the thermal conductivity, L is the length, A is the area, and ΔT is the

temperature difference. The heat was dispersed to the ambient from the cold side, which can be described by Equation (3):

$$Q_C = \mathrm{K}(T_C - T_{amb}) \tag{3}$$

where K is thermal conductance and T_{amb} is ambient temperature. The temperature difference (ΔT) between the hot and cold sides of the TEG is determined using Equation (4):

$$\Delta \mathrm{T} = T_H - T_C \tag{4}$$

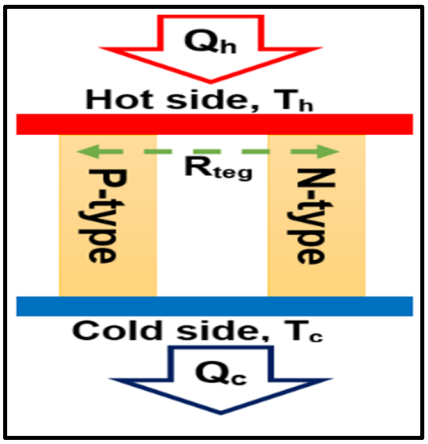

Figure 1. Schematic diagram of heat flux distribution of the TEG.

The current (I) in the module can be expressed by Equation (5):

$$\mathrm{I} = \frac{V_{oc}}{R_{TEG} + R_{load}} \tag{5}$$

The open-circuit voltage is calculated using Equation (6):

$$V_{oc} = \alpha \Delta \mathrm{T} \tag{6}$$

Optimum power output, P_{max}, is determined by Equation (7):

$$P_{max} = \frac{{V_{oc}}^2}{4R_{TEG}} \tag{7}$$

The efficiency of power transfer is obtained using:

$$\eta_P = \frac{P_{out}}{P_{TEG}} \times 100 \tag{8}$$

where P_{out} is the output power of the DC converter and P_{TEG} is the TEG input power

2.1. TEG in the Series Array Configuration

The internal resistance and Seebeck coefficient are assumed constant parameters in the series TEG configuration. The module may experience different temperatures under non-uniform heat flux conditions, $\Delta T_1, \Delta T_2, \ldots, \Delta T_{\mathrm{N}}$, respectively. Thereby, Equation (1) becomes Equation (9) due to the non-uniform heat flux condition. The heat balance at the cold side for each module is also different, as shown in Equation (10).

$$Q_{HN} = \alpha T_{HN} I + \left(\frac{\lambda A}{L}\right) \Delta T_N - 0.5 I^2 R_{TEG} \tag{9}$$

$$Q_{CN} = \alpha T_{CN} I + \left(\frac{\lambda A}{L}\right)\Delta T_N - 0.5 I^2 R_{TEG} \quad (10)$$

The heat dissipated to the ambient is expressed by Equation (11):

$$Q_{CN} = \mathrm{K}(T_{CN} - T_{amb}) \quad (11)$$

The open-circuit voltage and current were calculated using Equations (12) and (13), respectively:

$$V_{oc} = \alpha(\Delta \mathrm{T}_1 + \Delta \mathrm{T}_2 + \ldots \Delta \mathrm{T}_N) \quad (12)$$

$$\mathrm{I} = \frac{V_{oc}}{N R_{TEG} + R_{load}} \quad (13)$$

2.2. TEG in the Parallel Array Configuration

The heat balance equation in a parallel array configuration is similar to the series configuration. According to the Kirchhoff law, the relation of the current is $I = I_1 + I_2 + \ldots$ ..+ I_N. Thereby, the current is calculated using Equations (14) and (15):

$$\mathrm{I}_N = \frac{V_{ocN} - V_P}{R_{TEG}} \quad (14)$$

$$I = \frac{V_p}{R_{load}} \quad (15)$$

where V_p is the load resistance voltage. For maximum output power, the internal resistance is equal to the load resistance. Therefore,

$$R_{load} = \frac{1}{N} R_{TEG} \quad (16)$$

$$V_p = \frac{V_{oc1} + V_{oc2} + \ldots + V_{ocN}}{2_N} \quad (17)$$

3. Method and Instrument of Preliminary Work for Real-Time Data

The preliminary work of this research is illustrated in Figure 2. The characteristic of the temperature profile in real-time implementation should be considered to design the thermal energy harvesting circuit. Therefore, the process conducted to obtain all the necessary data to develop the harvesting circuit is briefly explained in this section.

An experiment was conducted at stage 1 to measure the temperature and the open-circuit voltage. The TEC1-12706 module (40 × 40 mm) parallel array configuration covers a roof area of 1 m^2. In addition, the module was sandwiched between the roofing material (hot side) and the aluminum heatsink (cold side). The heatsink is used for heat dissipation by nature wind blowing. A thermal paste (Cooler master HTK-002) increases the thermal conductivity at TEG hot and cold sides. Specific modules from National Instrument, NI-9211 (temperature) and NI-9201 (voltage), were used to measure the temperature and voltage. A K-type thermocouple was used to measure the hot and cold side temperatures. The measuring system was integrated with the NI cRIO-9014 controller module, which records all experiment data and synchronizes with the computer. LABVIEW software was used to design the layout for the data recording. The data were recorded for 24 h at every second interval for 20 days. The experiment shows the amount of a temperature difference at the TEG that can be harvested. Based on the experiment, the maximum temperature difference range is from 0.3323 °C to 0.4871 °C (morning, 12.00 a.m. to 6.00 a.m.), 0.3407 °C to 0.7842 °C (evening, 6.00 p.m. to 12.00 a.m.), and 2.0 °C to 6.072 °C (day, 6.00 a.m. to 6.00 p.m.). Refer to [2] for details. From the results, understanding the real-time temperature variation at TEG's hot and cold sides due to solar radiation in Malaysia was achieved.

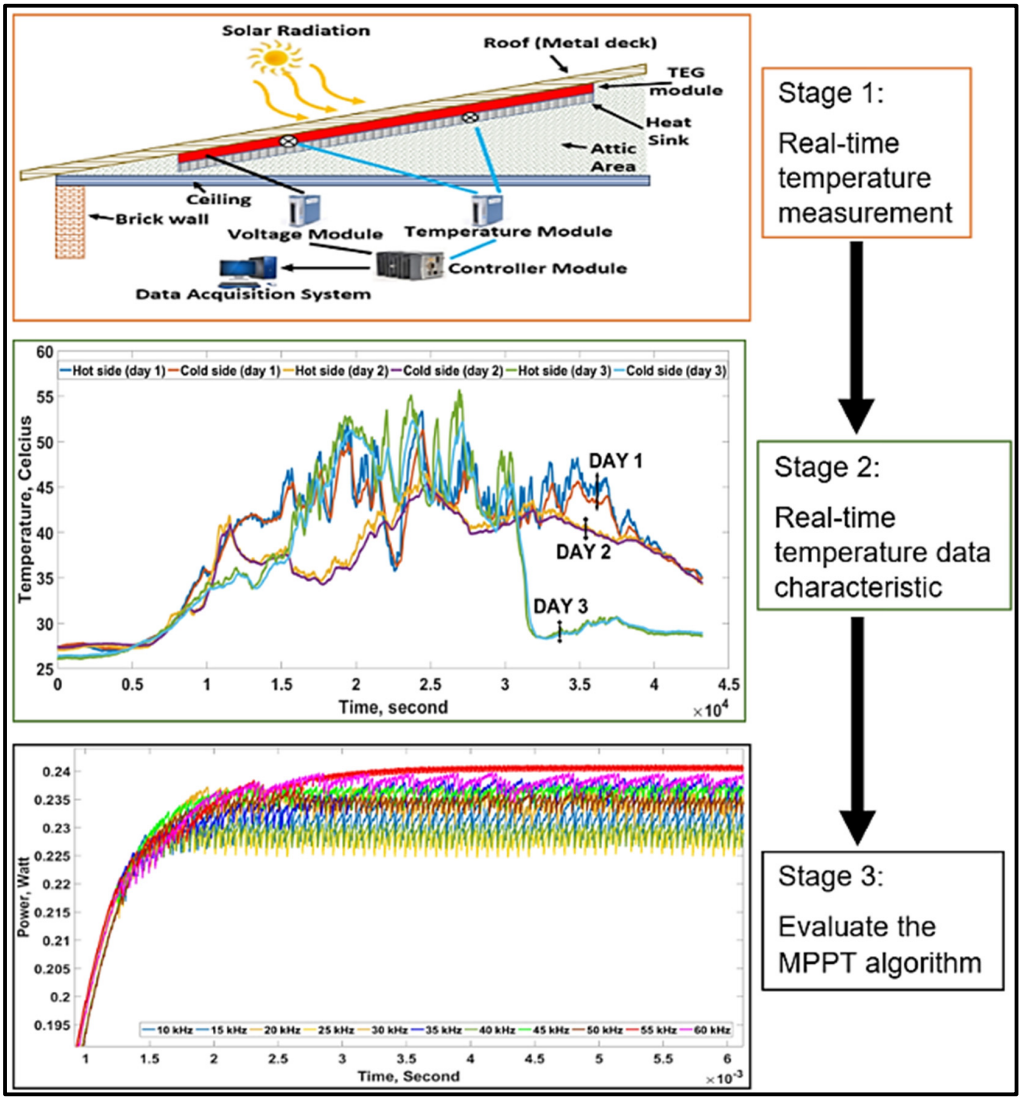

Figure 2. The stages of the preliminary experiment for real-time thermal energy harvesting.

From the experiment, the real-time temperature data show several characteristics: fluctuation, reverse conditions, low- and high-temperature differences, and sudden temperature changes. Concerning the experiment data, stage 2 is the evaluation of the temperature data at the TEG using MATLAB Simulink. First, real-time data were used in the simulation process. Then, the simulation protocol was designed to determine the TEG's open-circuit voltage at variable loads (90, 125, 200, 250, 503, and 600 Ω). From the analysis, the maximum voltage was proportional to the load value. Therefore, impedance matching was observed. In addition, the effect of the variable load to obtain the maximum power transfer was determined. Refer to [64] for details. At this stage, absolute data analysis (ADA), as shown in Figure 3, and synchronous data management methods were proposed to process the real-time temperature data due to the mixed data (positive and negative values), rapid temperature fluctuation, intersection point, temperature variation range, and reverse condition. Using the conventional method, the real-time data must be processed part-by-part, leading to technical errors when determining the exact point of reverse transition. Therefore, the ADA method was applied to the TEG equivalent circuit to obtain the statistical parameter of real-time data (~86,000 per day, 1,720,000 for 20 days) for further analysis. Compared to the conventional method [65], the ADA method indicates an accurate statistical parameter value. Using this method, rigorous analysis can be performed in terms of real-time data. Refer to [65] for the result.

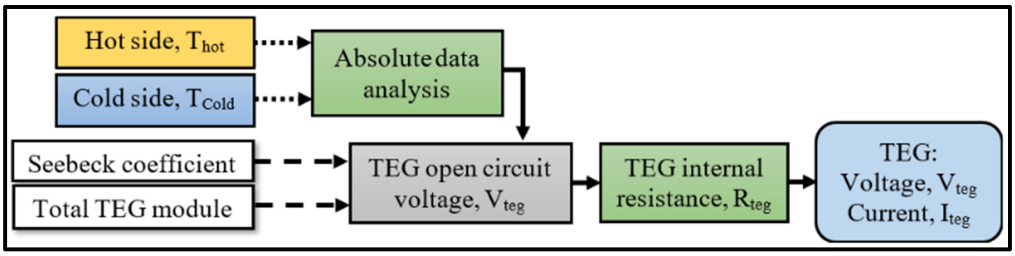

Figure 3. The block diagram of the ADA method of an equivalent TEG circuit.

The maximum power point (MPP) can be achieved by matching the impedance between the TEG internal resistance and the load. However, the real-time characteristic data makes it hard to achieve compared to constant temperature differences. Therefore, another option is to use the maximum power point tracking (MPPT) algorithm to track the MPP. The simple, fast response and ease of troubleshooting is the key to selecting the MPPT algorithm. However, the MPPT algorithm needs proper tuning, referring to the type of application, response time, parameter range, and input signal condition [66]. Thereby, the evaluation of the oscillation range, efficiency, and power losses of the MPPT algorithm is performed at stage 3. The frequency range of 10 to 60 kHz with 5 kHz increments was tested using the real-time temperature data. From the simulation, 55 kHz obtained the lowest oscillation range (0.0012), higher efficiency (84.12%), and the lowest power losses (4.55%) compared to other frequencies. Therefore, 55 kHz indicates the suitable frequency value for the controller.

Based on the simulation results from stage 1 to stage 3 of real-time data, the design and development of the TEHS, considering all the values, was fabricated for field tests (real-time implementation). Figure 4 presents the field test setup of the TEHS to harvest thermal energy from solar radiation. It consists of a TEG module, roofing materials, and the DLVB. The equipment setup was left exposed to solar radiation and weather changes to evaluate the effectiveness of TEHS in real-time conditions. The following section will briefly explain the design and development of the TEHS.

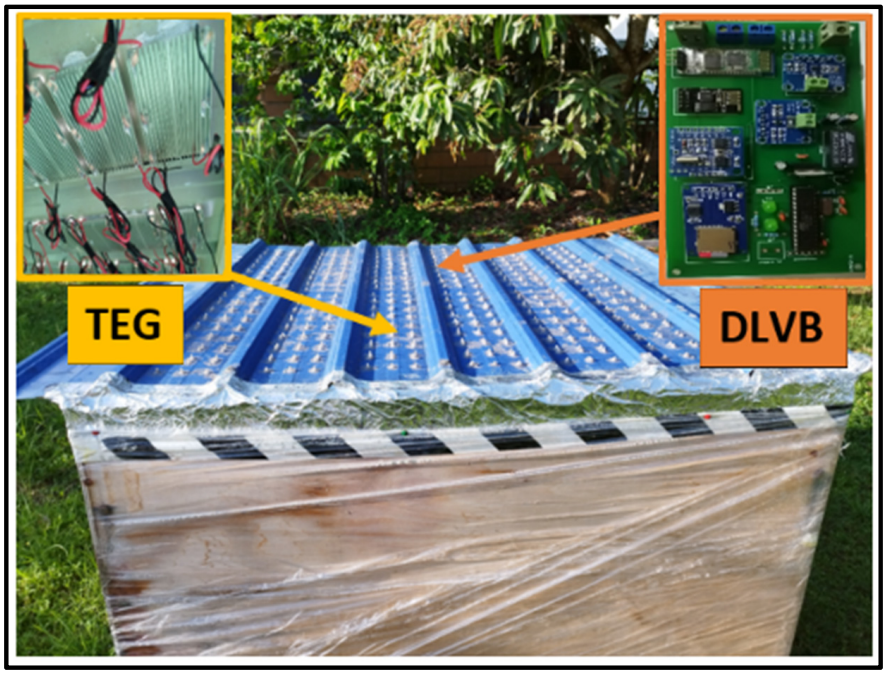

Figure 4. The real-time field test setup.

4. Energy Harvesting Circuit Design and Development

This section explains the design and development of the thermal energy harvesting circuit, including the working principle. This type of harvesting circuit is proposed based on the TEG input voltage characteristic discussed in Section 3.

4.1. Topology of the Harvesting Circuit

Figure 5 represents the stage of the proposed thermal energy harvesting circuit. Again, the DLVB is considered in designing the harvesting circuit, which is low voltage (<1 volt) and high voltage (>1 volt).

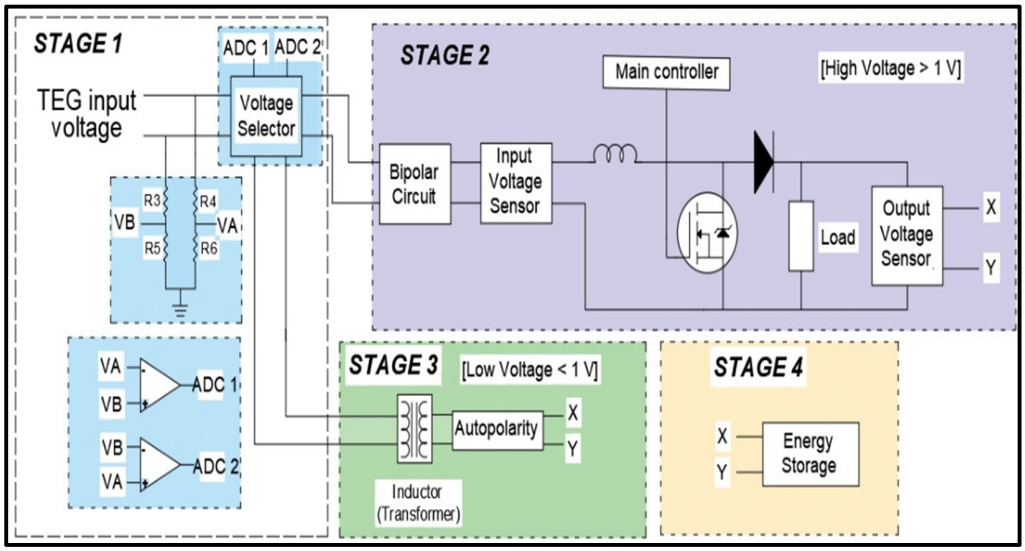

Figure 5. The stage of the thermal energy harvesting circuit.

At stage 1, the TEG input voltage is a random value depending on solar radiation and environmental conditions. It consists of low and high voltage, including the bipolar requirement for both voltage levels. Two operational amplifiers, ADC 1 and ADC 2, were used to detect the input value's level and condition, capable of categorizing the input (low and high voltage). It received the signal from VA and VB connected to the TEG input voltage with a voltage divider circuit. The value of R3 and R4 depends on the TEG input voltage. ADC 1 and ADC 2 transmit the data to the controller when the input value is confirmed. Then, the controller triggers the selector relay accordingly based on the programming setup. The initial position of the relay is connected to the low-voltage level circuit. When the voltage reaches a high-voltage level, the relay automatically switches to the high-voltage level circuit (stage 2).

In addition, the high-voltage level goes to the bipolar circuit before the DC boost converter. At this point, the bipolar circuit is compulsory due to the polarity of input voltage to the DC boost converter. Two voltage and current sensors at the input and output of the DC boost converter sense the voltage value and transmit it to the controller. Then, the MPPT algorithm programmed in the controller tracks the MPP. On the other hand, if the input voltage from the TEG is below 1 volt, the low-voltage level circuit will work (stage 3). This circuit consists of an inductor transformer integrated with a specified capacitor value. LTC 3109 (Texas Instruments) played a role in receiving and processing the input voltage value and amplifying the output depending on the VS1, VS2, and Vaux connection. The output voltage from both high and low circuits is stored in the storage component. Here, a 3.7-volt lithium-ion battery (4200 mAH) with a charger module (TP4056) was used (stage 4). The selection of energy storage considers several factors: self-discharge rate, charging and discharging characteristics, cycling stability, and price. The comparison of the storage element is briefly presented in Table 3.

Table 3. The comparison of selected parameters of a rechargeable battery and a supercapacitor.

Parameter	Rechargeable Battery	Supercapacitor
Charge/discharge efficiency	Low	High
Self-discharge rate	Low	High
Energy density	High	Low
Power density	Low	High
Charging circuit complexity	High	Low
Price vs. capacity	Low	High

4.2. Thermal Harvesting Circuit

The thermal energy harvesting circuit design comprises several modules combined on one board, as presented in Figure 6. PROTEUS software was used to design the harvesting circuit and the printed circuit board (PCB). The details of the components used in the harvesting circuit are listed in Table 4. The selection of each component used on the circuit board goes through comprehensive experimental testing to evaluate each module's robustness, endurance, and capability range. Furthermore, all the voltage and current values from the harvesting circuit are stored in the microSD card module, with 64 Gb capacity. Thus, expanding the amount of data stored for further analysis and the duration of the field test experiment. The real-time clock module (RTC 3231) records the present time of each piece of data.

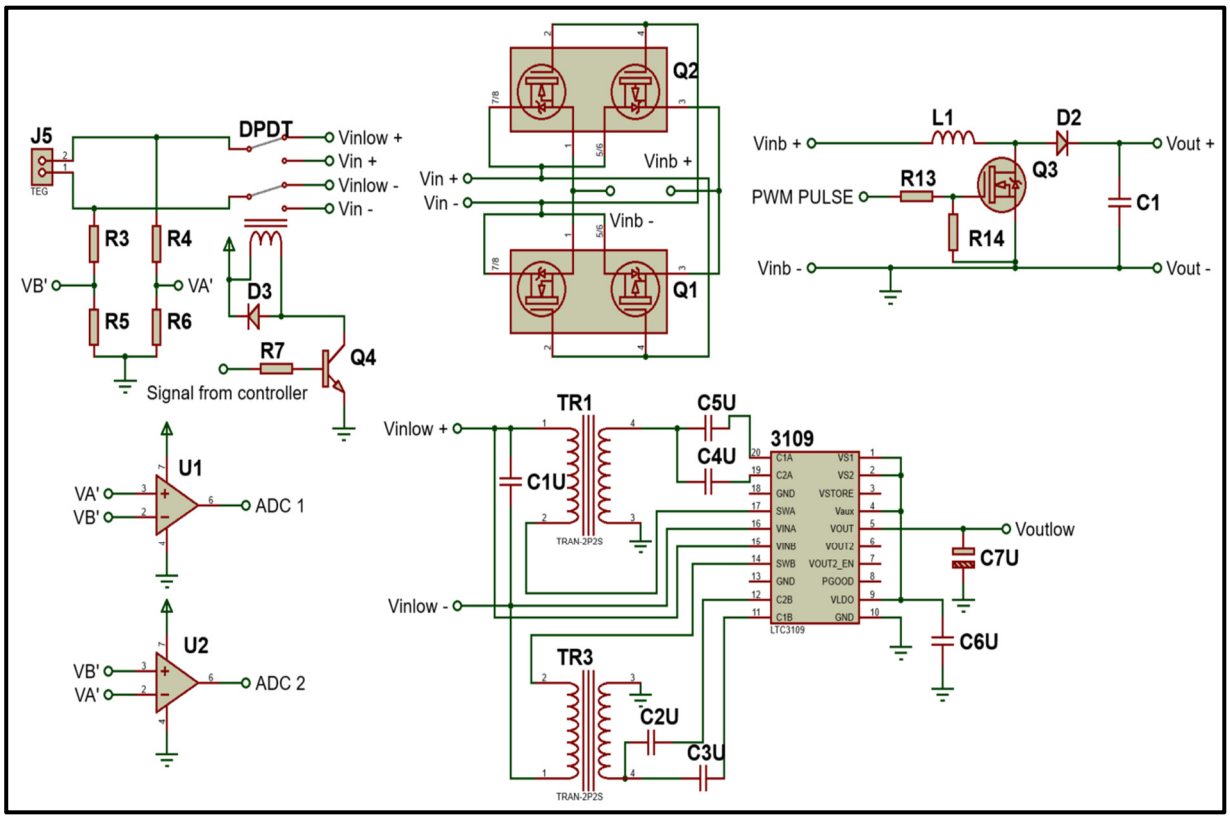

Figure 6. Schematic diagram of bipolar dual-level voltage circuits.

The input voltage from the TEG is connected to J5 without considering the electrical polarity. The voltage divider circuits VA and VB′ detect the input voltage value with the dual-polarity capability. Thus, the value was compared at ADC 1 and ADC 2. ADC 1 was connected to ADC 0 (pin23) and ADC 2 to ADC 1 (pin24) at the AT328 microcontroller. If the input voltage is positive at the VA and VB′ is negative, ADC 1 will send the signal to the controller. The process is reversed when the VA is negative and VB′ is positive—ADC

2 will send the signal to the controller. The signal from ADC 1 and ADC 2 is sent to the controller to evaluate and sent back to the DPDT relay circuit (signal from the controller). If the input voltage is below 1 volt, the relay switches to a low-voltage level circuit and vice versa. This process continuously occurs along the circuit work.

Table 4. Detailed descriptions of each component in the harvesting circuit.

Label	Module/Port	Description
U1, U2	Voltage signal	Gain at 5
ADC 1, ADC 2	Operational amplifier/Comparator	AD627
R3, R4	Resistor	1.5 KΩ
R5, R6	Resistor	100 Ω
R7	Resistor	1 KΩ
R13	Resistor	100 Ω
R14	Resistor	10 KΩ
DPDT	Double pole double throw relay	5 V
Q1, Q2	MOSFET	IRF7319
Q3	MOSFET	IRLZ44N
Q4	Transistor	BC548
D3	Diode	1N4148
D2	Diode	1N5817
L1	Inductor	100 µH
C1	Capacitor	47 µF
C1U	Capacitor	47 µF
C2U, C4U	Capacitor	470 pF
C3U, C5U	Capacitor	10 nF
C6U	Capacitor	1 µF
C7U	Capacitor	470 µF
TR1, TR2	Step-up transformer	25 µH
3109	Controller	LTC 3109
PWM Pulse	Gate controller	AT328 microcontroller with MPPT
INA 219	Voltage and current sensor	Serial connection to Vin+ and Vout+

The bipolar circuit (Q1 and Q2) at a high-voltage level circuit was used to change the electrical polarity accordingly before connecting to the DC boost converter circuit. Thereby, the polarity has followed the polarity at the DC boost converter. Therefore, a DC boost converter was selected to increase voltage levels from low to high. The drawback is that the current is decreased [67]. At this point, the voltage and current sensor module (INA 219) was used to trace the input voltage and current value, and thus sent to the controller. A similar process occurs at the output of the DC boost converter. Concerning the sensor's input and output voltage values, the controller's MPPT algorithm will evaluate both values and adjust the duty cycle to track the maximum power point (MPP). Then, pulse width modulation (PWM) works according to a new value to control the MOSFET. Resistors (R13 and R14) ensure that the MOSFET gate is fully closed to prevent switching losses.

For low-input voltage (Vinlow), two step-up transformers with a coil ratio of 1:20 with coupling capacitors (C2U, C3U, C4U, and C5U) allow it to boost the input voltage. Typically, the oscillation frequency is determined by the inductance transformer secondary winding from 10 to 100 kHz. LTC 3109 can accurately regulate the output voltage when the Vaux is 2 V. The VS1 and VS2 at the LTC 3109 pin were tied to Vaux to achieve 5 V of the output voltage (Voutlow).

Preliminary testing of the harvesting circuit has been conducted to evaluate the functionality and performance of the proposed system for real-time implementation. DC power supply (GPC-3020, GW INSTEK) was used as the input voltage at J5. The voltage range was from 0.2 to 4 V, with a 0.2 V interval. The current from the DC power supply was set at

100 mA. Regarding voltage fluctuation from the preliminary experiment, the testing time duration for each voltage range was 10 s (constant time), with various time intervals.

5. Result

This section presents and discusses the experimental testing result of the thermal energy harvesting circuit component. The experimental method was chosen to evaluate the performance and endurance of each component according to the input voltage from the TEG to prove the component's reliability in dealing with the fluctuation and reverse polarity of the TEG input voltage. Furthermore, a comparison among the component types was accomplished through the experimental method.

5.1. Individual Stage Experimental Testing

Figure 7 shows the voltage selector switching result based on the normal (N) and reverse (R) polarity tested according to the TEG input voltage from 0.1 to 5 V. As a result, the V_A obtained a positive projection proportional to the increasing input voltage, while V_B remained at zero value. In contrast, V_B behavior was parallel to the increase of the input voltage. Therefore, a response between V_A and V_B related to the TEG input voltage condition was observed.

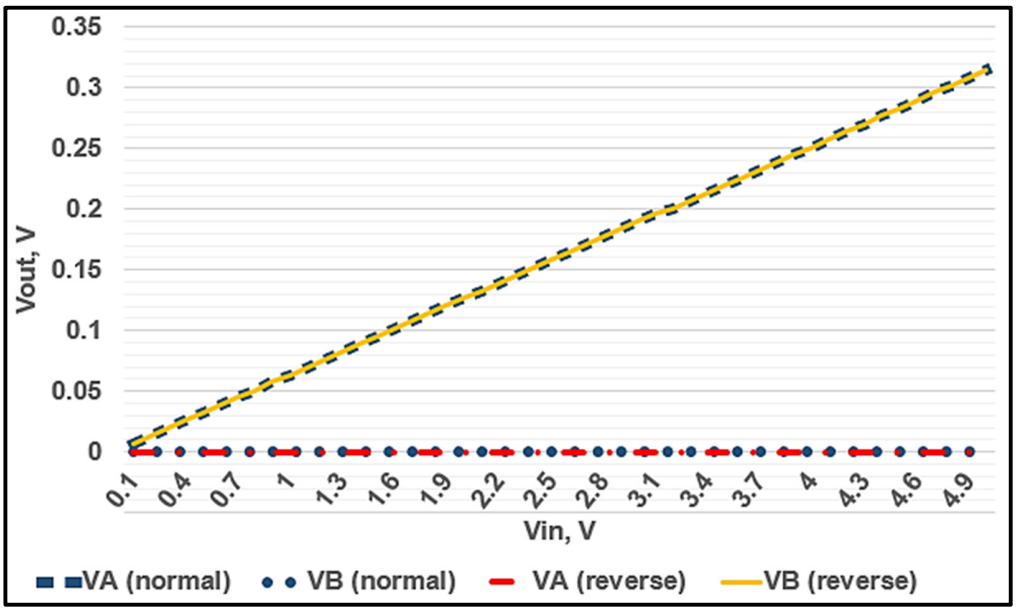

Figure 7. Voltage selector switch.

The experimental result of IRF7319 consists of a combination of P- and N-channels for the bipolar circuit, as shown in Figure 8. The MOSFET was tested at normal and reverse polarity to evaluate the output voltage from the MOSFET. The result indicates that the minimum voltage was 1 volt, achieved without losses compared to a voltage range below 1 volt. At the low-voltage level, the MOSFET indicated the losses with a maximum value of 30% obtained at 0.4 volts. However, the losses did not affect the implementation of the circuit because this bipolar circuit was used at a high-voltage level (>1 V). Thereby, the performance of the MOSFET achieved 100%.

Figure 9 presents the results of three different types of MOSFETs used in the DC converter circuit. IRLZ44N indicated a higher performance compared to IRF540N and IRFZ44N. IRLZ44N is a logic-level MOSFET, requiring a minimum gate-source voltage (V_{GS}) of 1 volt to operate. In contrast, IRF540N and IRFZ44N required a minimum V_{GS} of 2 volts. Therefore, it afforded the MOSFET and the DC converter circuit advantages to boost the voltage at a specific level. For example, at 0.5-volt, equivalent output voltage was

obtained from all the MOSFETs and increased for each voltage increment. From 1 to 4 volts, IRLZ44N performed well in the task as the switching component in the DC boost converter.

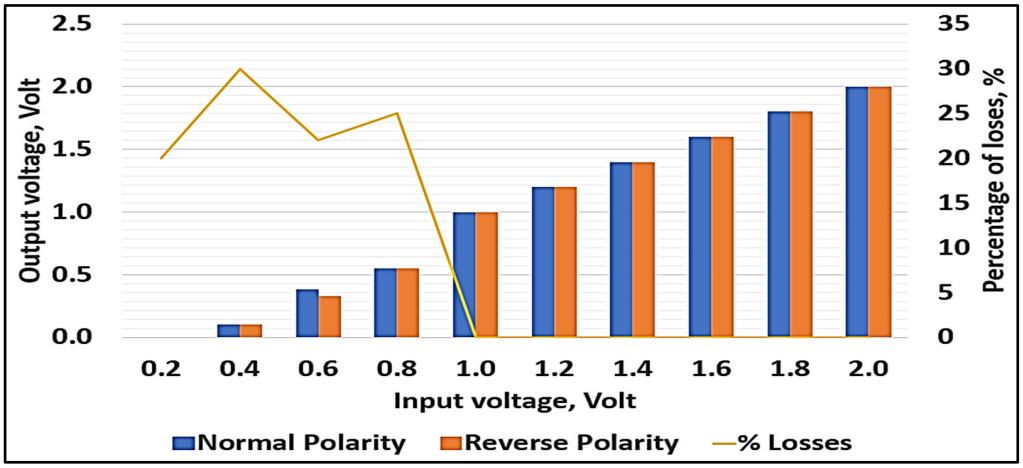

Figure 8. Bipolar circuit result.

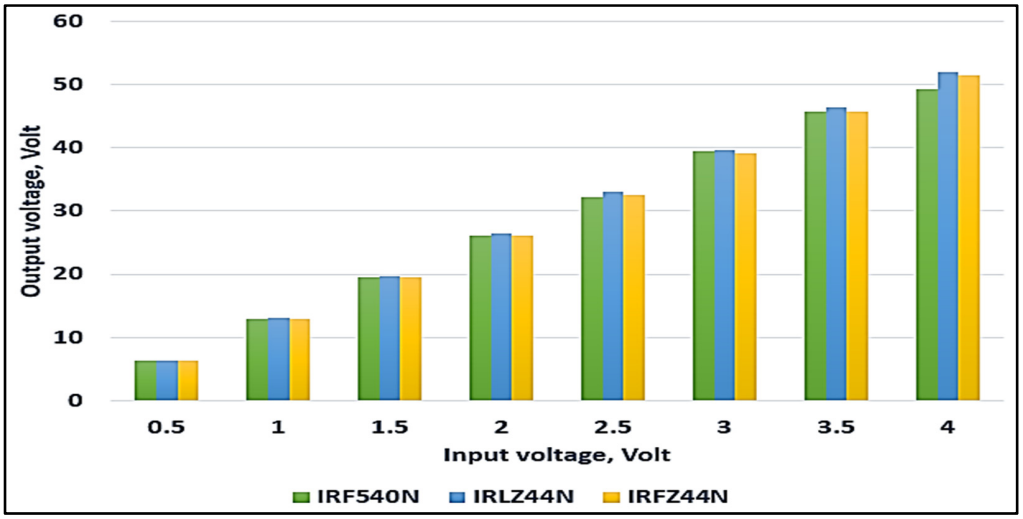

Figure 9. Comparison of MOSFETs used in the DC converter.

Furthermore, the DC boost converter circuit was tested at different duty cycle values from 0.2 to 0.8 to evaluate the circuit's efficiency and endurance, as shown in Figure 10. In addition, the input voltage range was between 0.2 V and 10 V, with a MOSFET switching frequency value of 55 kHz. From the experimental testing, the 0.2 duty cycle obtained a constant efficiency of 80% from 1.8 volts, with a maximum efficiency of 95.7% at 10 V. Compared to 0.4 duty cycle value, the maximum efficiency is 89.5%. In contrast, 0.7 and 0.8 duty cycle values caused failure in the load resistance at 5.8 and 4.2 V, respectively.

5.2. Circuit Experimental Test

The TEG high- and low-voltage levels were extracted from the experimental results and plotted for comparison. For a clear view of the voltage generated from the harvesting circuit, the low and high voltages are plotted in Figure 11. It is seen that the low- and high-voltage level circuits can boost the input voltage at different capabilities. Although the low-voltage circuit directly implemented the on-shelf component, it fulfilled the circuit design's objective to harvest thermal energy at the low-voltage level. The low-voltage level circuit indicates that the voltage can be above 3.6 V at 0.6 to 0.8 V.

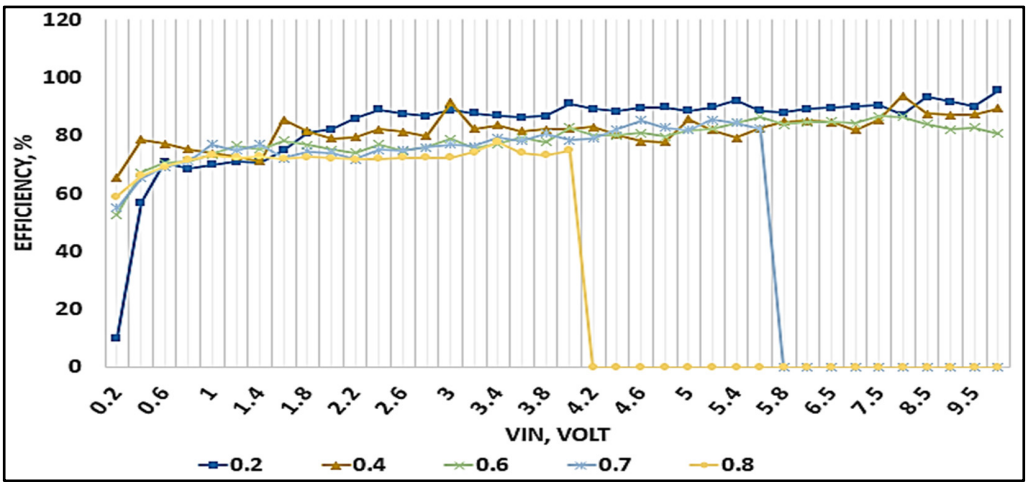

Figure 10. Comparison of the DC converter duty cycles.

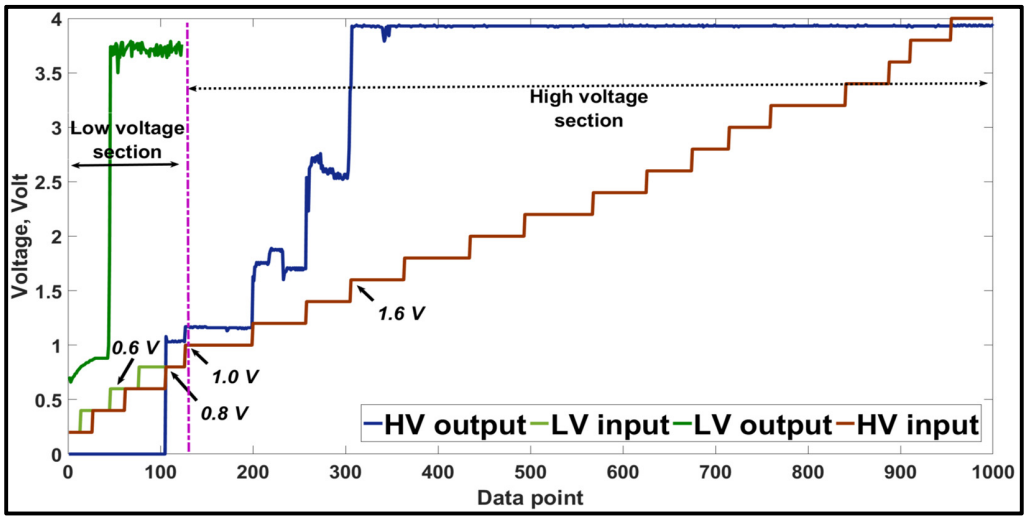

Figure 11. Input and output voltage from the low- and high-voltage levels.

A high-voltage level DC converter indicates a good response to boost the input voltage above 1 V. It was observed that starting from 1.6 V, the voltage increased above 3.5 V and was constant along the increase of the input voltage. At this point, it was observed that the battery was in changing state. Furthermore, when using the battery as the load, the output voltage of both low- and high-voltage level circuits was capped at approximately 4 V. It is aligned with the nominal battery voltage at 3.6 V [68].

Moreover, the current indicates the increasing value proportional to the voltage, as presented in Figure 12 The range at low-voltage levels was from 0.1 to 0.8 mA. While, for high-voltage levels, the current achieved 12 mA. The importance of the current value is to determine the potential to charge the battery. Although the voltage is high, it is not guaranteed to charge the battery without enough current, thus affecting the charging time. The current trend is aligned with the theoretical aspect, which is proportional to the voltage increase.

On the other hand, the harvesting circuit testing not only focused on the voltage and current values but also considered the duty cycle response to the present input value. The controller used the MPPT algorithm to track the MPP by adjusting the duty cycle based on the present input and output values, as shown in Figure 13. The duty cycle was at a steady state (point 1 and 1′) until a sudden increment of the input voltage value from 0.79 (point 1) to 1.26 V (point 2) occurred. In addition, the response of the duty cycle from 18 (point 1′) to 16 (point 2′) is in good agreement with the present value to track the MPP. Moreover,

the present input value decreased from 1.26 (point 2) to 1 V (point 3), and the duty cycle tended to increase the value from 16 (point 2′) to 18 (point 3′). Then, the duty cycle was constant at 16 (point 4′) due to the constant input value. Significantly, there was no lagging between the input voltage and the duty cycle response. Therefore, tuning the duty cycle for further implementation in real-time behavior is achievable.

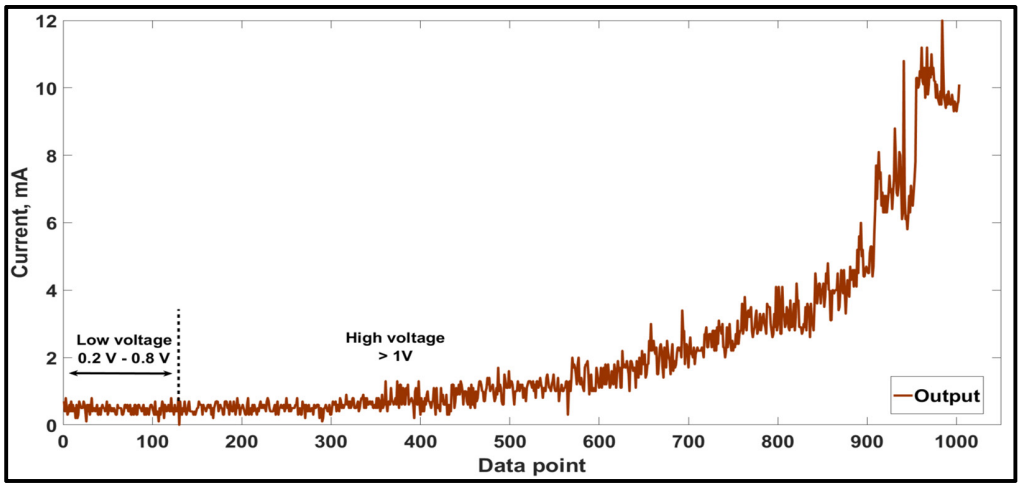

Figure 12. The output current of low- and high-voltage levels.

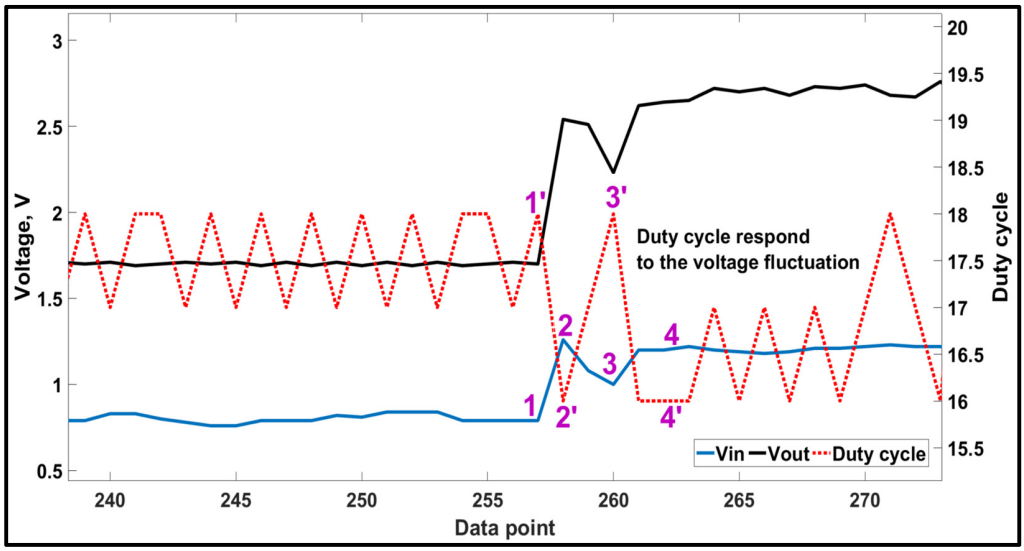

Figure 13. The duty cycle responds to the fluctuation of the input voltage.

Moreover, the overall data of the harvesting circuit is plotted in Figure 14, focusing on the harvesting circuit's efficiency. The time for each voltage level was not set to constant time, and it varied to show an overview of the system response. As discussed previously with the voltage result, the output voltage achieved above 3.5 V at a 1.6 V input voltage. The output voltage was constant above 3.5 V until the input voltage was 4 V. For this setup, the mean efficiency of the harvesting system was 91.92%.

5.3. Circuit Field Test

Further, the DLVB was tested at the field test of real-time implementation to evaluate the output from the TEG. In addition, the performance of the DLVB can be determined by referring to the fluctuation of the temperature difference. At this point, the DLVB was fully exposed to the present solar radiation and weather conditions for 51 days. Therefore, the mean of input and output voltage results is presented in Figure 15. Based on the graph, the

input voltage range was from 1.245 (day 18) to 3.437 V (day 6). For the output voltage, the range was 2.099 (day 22) to 3.847 V (day 42).

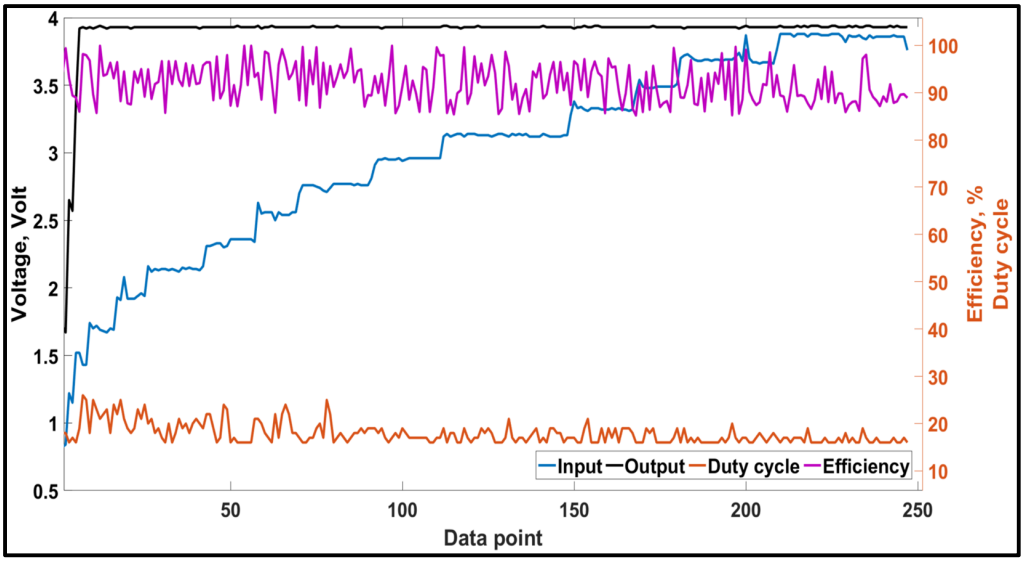

Figure 14. The input and output voltages, duty cycle, and efficiency of the harvesting circuit at various voltages and timeframes.

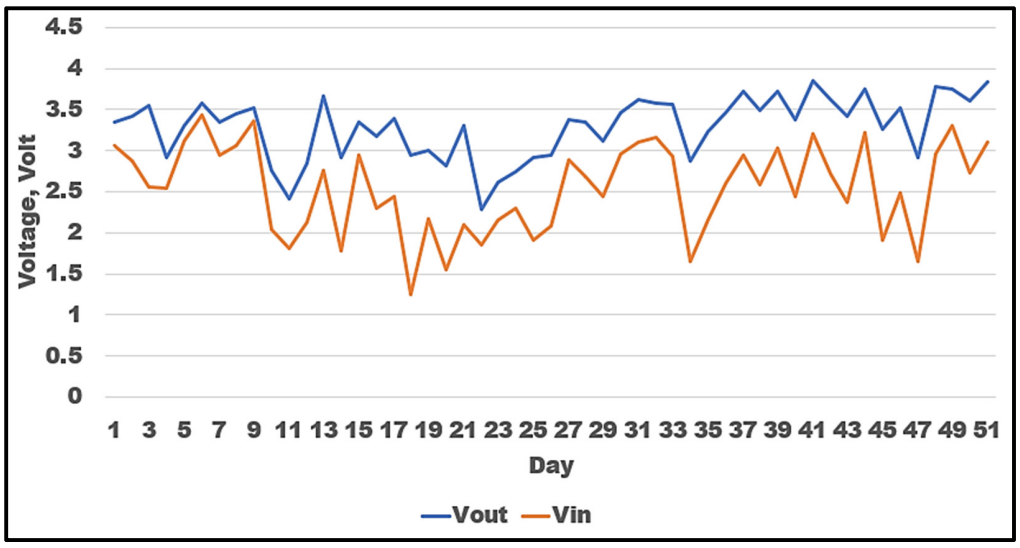

Figure 15. Mean voltage of real-time field test.

Moreover, the mean input and output currents are shown in Figure 16. The maximum mean input current obtained was 18.78 mA (day 9), with a minimum of 1.066 mA (day 11). In addition, the maximum mean output current was 16.64 mA (day 9), and the minimum was 0.464 mA (day 18).

Figure 17 presents the mean input and output power. The maximum mean output power was 66.1 mW (day 9), and the minimum mean output power was 1.45 mW (day 18). Further, the maximum mean input power was 74.1 mA (day 9), and the minimum mean input power was 1.56 mA (day 18).

The efficiency of the TEHS in the field test is portrayed in Figure 18. The maximum mean efficiency was 92.98% (day 43), and the minimum efficiency was 89.62% (day 9).

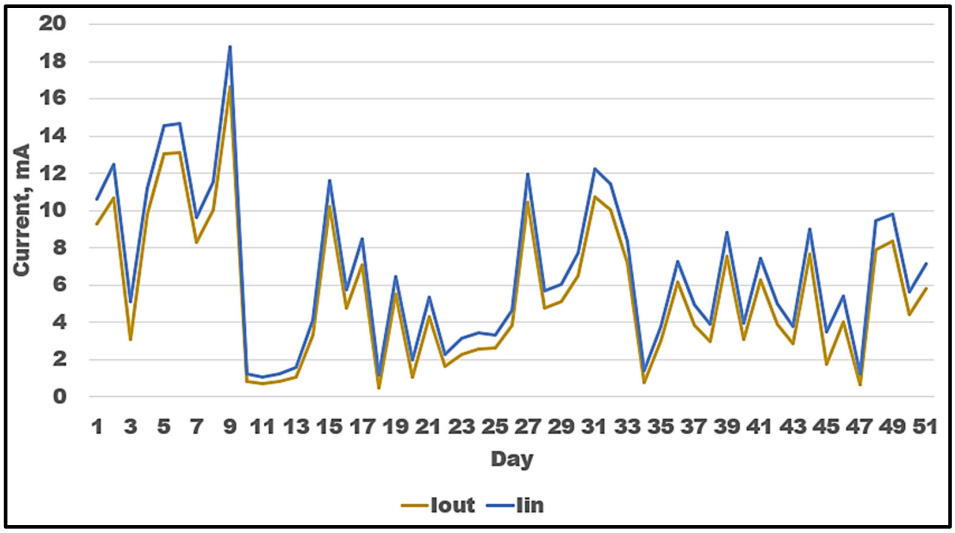

Figure 16. Mean currents of the real-time field test.

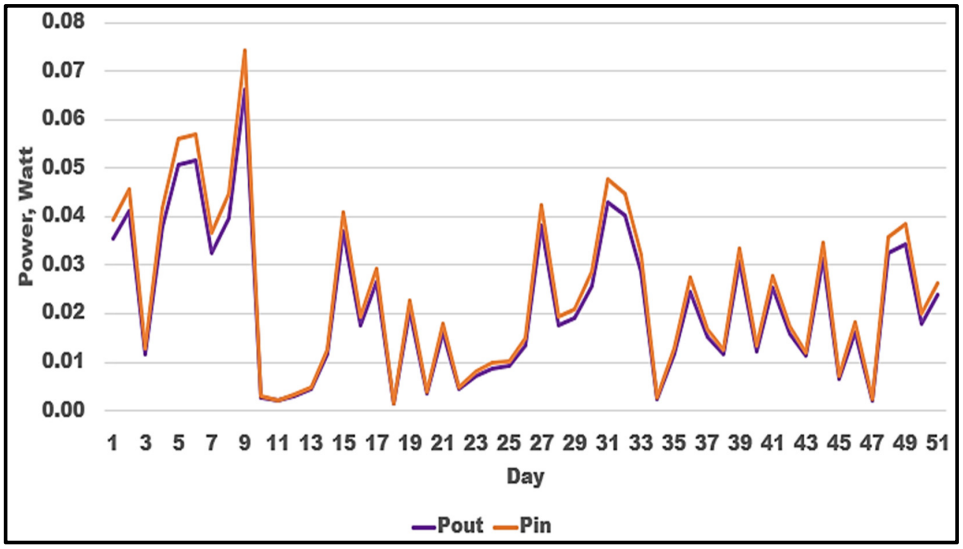

Figure 17. Mean power of the real-time field test.

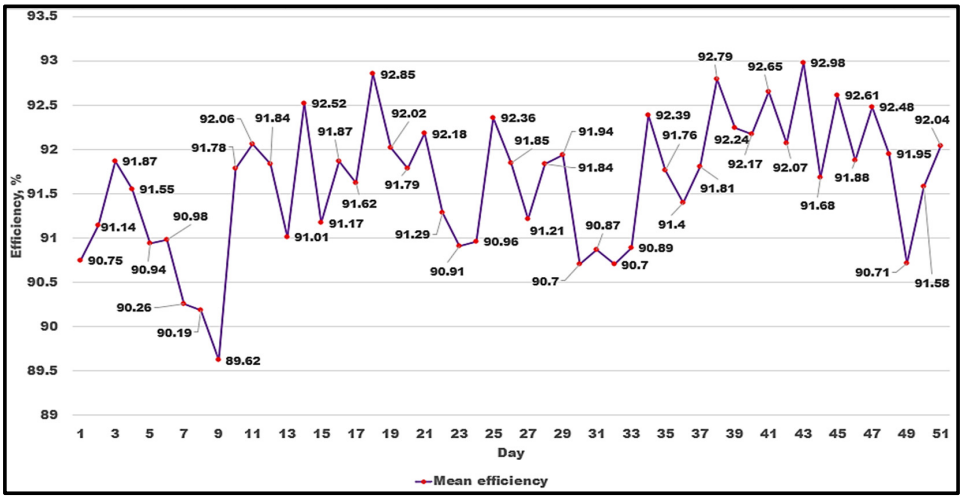

Figure 18. Mean efficiency of the real-time field test.

6. Discussion

Typically, research related to TEG is categorized into three interdependent domains: (a) improvement of material science, (b) the adaptation of the TEG at the lowest possible degradation compared to its nominal performance, and (c) implementation of the TEG and ways to improve TEG systems considering the demands of those applications [22]. Harvesting the thermal energy in a real-time situation is challenging. Therefore, many parameters should be considered when designing and developing the thermal energy harvesting system (TEHS).

The comprehensive preliminary work has been conducted and divided into three stages. The brief explanation regarding the method and instrument of the preliminary work was in Section 3, where the setup implementation focused on thermal energy from the roofing materials due to solar radiation and environmental conditions in Malaysia. From the simulation result, a temperature difference was obtained in the range of 2 to 6 °C (day), 0.3323 °C to 0.4871 °C (morning), and 0.3407 °C to 0.7842 °C (evening). According to the previous research, research at a low-temperature difference has been performed to evaluate the potential energy. However, certain research only measures the TEG's open-circuit voltage, especially for the roofing material. In addition, the researchers reported an output power value of 65.22 μW at 138 Ω (ΔT = 3 °C).

Theoretically, a low temperature produces a low output power, thus limiting the generated power usage. Typically, a DC boost converter is a solution to the problem by increasing the input power. Therefore, a TEHS is necessary to design and develop based on the local environment to boost the input value with a load. In addition, the switching in the DC boost converter must be tuned according to the input parameter [69,70]. Thereby, the tuning of the frequency and duty cycle of the MPPT algorithm is conducted. The input signal to the controller is from the voltage and current sensor. Here, 55 kHz indicates the suitable frequency to implement with a 0.012 oscillation range, 4.55% power losses, and 84.12% efficiency. The result was compared with the frequency range from 10 to 60 kHz, with a 5 kHz increment.

In a real-time application, the temperature varies depending on the amount of solar radiation and weather conditions. Thus, it will affect the output voltage from the TEG. In addition, the output voltage from the TEG has several characteristics: the fluctuation of the voltage level and reverse polarity. Thus, the TEG can be used in various fields if there is a temperature difference between the hot and cold sides. Concerning the implementation of the TEG, a DLVB harvesting circuit was proposed in this work to maximize energy harvesting.

Further, the voltage divider will sense the input voltage from the TEG at a positive and a negative value. At this point, ADC 1 and ADC 2 transmit the input signal to the controller. Then, the selector relay will trigger according to the present input voltage value from the low- to the high-voltage circuit. The low-voltage circuit indicates that the voltage achieved a 3.5 V output voltage starting a from 0.6 V input voltage. Below 0.6 V, the voltage increased, but not enough to charge the battery. It can be seen in Figure 11 that the low-voltage circuit changed to a high-voltage circuit at 1 V. Thereby, the objective of the dual-level circuit was achieved. For the high-voltage circuit, the converter can boost the input voltage starting from 1 V. At this point, there is not enough voltage to charge the battery. When the input voltage increased at 1.6 V and above, the output voltage was constant above 3.5 V. Therefore, starting from 1.6 V, the output voltage can charge the battery.

The output current from the converter showed an increasing trend parallel to the increase in voltage. However, in a real-time application, the TEG's internal resistance was affected by the present temperature [71]. Therefore, the impedance matching between the TEG and the load varied. The MPPT algorithm was used in the controller to track the MPP value in the circuit. The MPPT will adjust the duty cycle according to the input and output values. The duty cycle response to the input and output value variation showed a good agreement, as depicted in Figure 13. The MPPT algorithm continuously tracks the MPP

along the fluctuation of input and output values. Therefore, the duty cycle will respond with no lag if there is a sudden increase or decrease in the value. On the other hand, the circuit is tested by increasing the voltage without the time duration for each voltage range to evaluate the duty cycle response and efficiency. The result indicated that the mean efficiency was 91.92%.

On the other hand, the TEHS was applied to the field test to evaluate the setup's performance. The setup was tested for 51 days, facing a variation of solar radiation and environmental changing. Field test results indicated that the mean output voltage range was 2.099 V to 3.847 V, mean output current was 0.464 mA to 16.64 mA, and mean output power was 1.45 to 66.1 mW. In addition, the mean efficiency of the TEHS was from 89.62% to 92.98%. Although the field test duration was 24 h, the temperature difference at night was below 1 °C, not enough to generate the output from the TEG. The comparison of the proposed TEHS with other studies is listed in Table 5.

Table 5. Comparison of low-temperature difference thermal energy harvesting.

Ref	[72]	[73]	[74]	[75]	[76]	This work
ΔT, °C	NA	9.5	4 and 12	5	6	6
Input	+1.0 and −1.0 V	0.7 V	−1.73 and −0.238 V	+1.5 and −1.5 V	0.4 V	1 V < Vin > 1 V (dual-level voltage)
Output	2.4 V	2.4 V	1.2 V	2.4 V	6.3 and 27.2 mW	4 V 1.45 to 66.1 mW
DC converter	Boost	Boost	Buck-boost	Boost	Boost	Boost
MPPT	Yes	Yes	Yes	Yes	Yes	Yes
Unipolar /Bipolar	Bipolar	Bipolar	Bipolar	Bipolar	Unipolar	Bipolar
Additional component	NA	NA	NA	NA	Radiator, thermal harvester	NA
Application	Exp.	Exp.	Exp.	Exp.	Real-time	Real-time

NA—not applicable, Exp.—experimental.

To estimate the potential of power generated from the result, considering the lowest mean power was 1.45 mW with an area of 1 m^2, the power output per square meter, P_{TEHS}, was determined by:

$$P_{TEHS} = \frac{P_{mean}}{A_R} = \frac{1.45\ mW}{1\ x\ 1} = 1.45\ \mathrm{mW/m^2} \quad (18)$$

where A_R is the area of TEG.

If the TEHS was used at 5 m^2 using a similar setup, the power production, P_P, would be calculated as follows:

$$P_P = P_{TEH}(A_R) = 1.45\ \times\ 10^{-3}\ (5) = 7.25\ \mathrm{mW} \quad (19)$$

Thereby, the generated power over 12 h (43,200 s) would be:

$$P_P(43200) = 313.2\ \mathrm{J} \quad (20)$$

On the other hand, the potential of output power can be utilized for wireless sensor nodes (WSN) and wireless data transmission. The average power demand of a WSN at the operating stage is 100 μW [77]. Therefore, the lowest mean output power can be used for 145 units of WSN. Furthermore, the wireless data transmission consisting of SHT31A-DSI-B (ambient temperature and humidity sensor), DS18B20 (soil temperature sensor), and DASH7 (transceiver module) required 3.3 V. In addition, the system consumes 900 μJ

(sensing) and 11.5 mJ (transmit 6 bytes) [78]. Therefore, referring to the energy generated, the system can be used continuously without any distractions.

7. Conclusions

This research evaluated the energy harvesting circuit system to harvest thermal energy from solar radiation on the roofing material. The preliminary work was briefly explained in Section 3. The temperature differences recorded from the experiment were 0.3323 °C to 0.4871 °C (morning, 12.00 a.m. to 6.00 a.m.), 0.3407 °C to 0.7842 °C (evening, 6.00 p.m. to 12.00 a.m.), and 2.0 °C to 6.072 °C (day, 6.00 a.m. to 6.00 p.m.). The design and development of TEHS were according to the local solar radiation and environmental conditions to implement it in real-time application. Therefore, it was experimentally tested to evaluate its functionality and efficiency. Two different test approaches were used: (a) constant time and (b) varied time duration. The voltage range was from 0.2 to 4 V, with a 0.2 V interval. The results from the experiment show that the circuit design can detect, process, and function at a dual-level voltage. From the experimental testing, TEHS was seen to boost the voltage of a low-level circuit from 0.6 V. In comparison, a high-level circuit from 1.6 V obtained 3.6 V. Furthermore, the mean efficiency of the DC boost converter circuit was 91.92% for various time intervals. Therefore, the proposed TEHS can harvest thermal energy at different solar radiation levels and weather conditions. The field test result indicated that the mean output voltage range was 2.099 to 3.847 V, the mean output current was 0.464 to 16.64 mA, and the mean output power was 1.45 to 66.1 mW. In addition, the mean efficiency was from 89.62% to 92.98%.

8. Directions for Future Research

Based on the experimental and field test results, the recommendations for future research are as follows:

- Comparison of different roofing materials to harvest thermal energy.
- The development of integrated TEHS and roofing materials for flexibility, mobility, and ease of installation.
- Integrate the TEHS system with IoT technology.

Author Contributions: Conceptualization, M.A.J. and O.M.F.M.; methodology, M.N.R. (Muhammad Nazri Rejab) and M.A.J.; software, M.N.R. (Muhammad Nazri Rejab) and M.N.R. (Mohamed Najib Ribuan); validation, M.A.J., M.N.R. (Mohamed Najib Ribuan) and O.M.F.M.; formal analysis, M.N.R. (Muhammad Nazri Rejab) and M.A.J.; investigation, M.N.R. (Muhammad Nazri Rejab) and M.N.R. (Mohamed Najib Ribuan); resources, O.M.F.M.; data curation, O.M.F.M. and M.N.R. (Muhammad Nazri Rejab); writing—original draft preparation, M.N.R. (Muhammad Nazri Rejab), M.A.J., M.N.R. (Mohamed Najib Ribuan) and O.M.F.M.; writing—review and editing, M.A.J., M.N.R. (Mohamed Najib Ribuan) and O.M.F.M.; visualization, M.N.R. (Mohamed Najib Ribuan); supervision, O.M.F.M.; project administration, M.A.J.; funding acquisition, O.M.F.M. and M.A.J. All authors have read and agreed to the published version of the manuscript.

Funding: This research was funded by the Ministry of Higher Education (MOHE) through the Fundamental Research Grant Scheme (FRGS/1/2018/TK10/UTHM/02/2) or Vot No. K108.

Institutional Review Board Statement: Not applicable.

Informed Consent Statement: Not applicable.

Data Availability Statement: Not applicable.

Conflicts of Interest: The authors declare no conflict of interest.

Abbreviations

Nomenclature

RE	Renewable energy
FiT	Feed-in-Tariff
NEM	Net energy metering
PCM	Phase change material
ZT	Figure of merit
TEHS	Thermal energy harvesting system
TEG	Thermoelectric generator
LV	Low voltage
STEG	Solar thermoelectric generator
Voc	Open-circuit voltage
TEH	Thermal energy harvesting
CPV	Concentrated photovoltaic
CPVT	Concentrated photovoltaic thermal
MCHP	Micro-channel heat pipe
DC	Direct current
HV	High voltage
PCB	Printed circuit board
PV	Photovoltaic
TEM	Thermoelectric generator module
DLVB	Dual-level voltage bipolar
MPPT	Maximum power point tracking
ZCS	Zero-crossing switch
DCM	Discontinuous mode
ADA	Absolute data analysis
MPP	Maximum power point
PCB	Printed circuit board
DPDT	Double-pole double-throw
PWM	Pulse width modulation

Symbol

Q_H	Heat source
Q_C	Heat dispersed
R_{TEG}	TEG internal resistance
T_H	Hot side temperature
T_C	Cold side temperature
ΔT	Temperature difference
T_{amb}	Ambient temperature
I	Current
R_{load}	Load resistance
V	Voltage
P_{max}	Maximum power
η_p	Power efficiency
P_{out}	Output power
P_{TEG}	TEG input power
N	Number of TEG modules

Subscript

oc	Open-circuit
°C	Degrees Celsius
μ	Micro
W	Watt
mW	milliwatt
Ω	Ohm
H	Hot
C	Cold
V	Volt

Greek symbol	
α	Seebeck coefficient
λ	Thermal conductivity
K	Thermal conductance

References

1. Zulakmal, M.Y.; Fudholi, A.; Rukman, N.S.; Nazri, N.S.; Yen, C.H.; Asim, N.; Mat, S.; Sopian, K. Computational fluid dynamics analysis of thermoelectric generators performance under solar photovoltaic-thermal (PVT) system. *J. Adv. Res. Fluid Mech. Therm. Sci.* **2019**, *56*, 223–232.
2. Rejab, M.N.; Johar, M.A.; Wan Jamaludin, W.A.; Saleh, U.A. Rooftop and Attic Area Thermal Energy from Solar Radiation as Renewable Energy in Malaysia. In Proceedings of the 2021 9th International Conference on Smart Grid and Clean Energy Technologies (ICSGCE), Sarawak, Malaysia, 15–17 October 2021.
3. Imran, M.; Alafiza, N.; Zafuan, A.; Kaassim, M.; Hashim, M. Pathways and challenges of solar thermal utilisation in the industry: ASEAN and Malaysia scenarios. *Sustain. Energy Technol. Assess.* **2022**, *52*, 102046.
4. Félix-Herrán, L.C.; García-Juárez, A.; García-Delgado, L.A.; González-Aguayo, P.S.; Lozoya-Santos, J.D.J.; Noriega, J.R. Characterization System for Heat-Energy to Electric-Energy Conversion from Concrete by Means of a Thermoelectric Module. *Sensors* **2022**, *22*, 1881. [CrossRef] [PubMed]
5. Gautam, A.; Chamoli, S.; Kumar, A.; Singh, S. A review on technical improvements, economic feasibility and world scenario of solar water heating system. *Renew. Sustain. Energy Rev.* **2017**, *68*, 541–562. [CrossRef]
6. Rimar, M.; Fedak, M.; Vahovsky, J.; Kulinov, A.; Oravec, P.; Kulikova, O.; Smajda, M.; Kana, M. Performance evaluation of elimination of stagnation of solar thermal systems. *Processes* **2020**, *8*, 621. [CrossRef]
7. Sun, Z.; Luo, D.; Wang, R.; Li, Y.; Yan, Y.; Cheng, Z.; Chen, J. Evaluation of energy recovery potential of solar thermoelectric generators using a three-dimensional transient numerical model. *Energy* **2022**, *256*, 124667. [CrossRef]
8. Shoeibi, S.; Kargarsharifabad, H.; Sadi, M.; Arabkoohsar, A.; Mirjalily, S.A.A. A review on using thermoelectric cooling, heating, and electricity generators in solar energy applications. *Sustain. Energy Technol. Assess.* **2022**, *52*, 102105. [CrossRef]
9. Javadi, M.A.; Ahmadi, M.H.; Khalaji, M. Exergetic, economic, and environmental analyses of combined cooling and power plants with parabolic solar collector. *Environ. Prog. Sustain. Energy* **2020**, *39*, 13322. [CrossRef]
10. Kabeel, A.E.; Abdelgaied, M.; Harby, K.; Eisa, A. Augmentation of diurnal and nocturnal distillate of modified tubular solar still having copper tubes filled with PCM in the basin. *J. Energy Storage* **2020**, *32*, 101992. [CrossRef]
11. Srivastava, S.; Deepak, C.S. Application of nano-PCMs in solar Photovoltaic. *J. WEENTECH Proc. Energy* **2020**, *6*, 47–58. [CrossRef]
12. Mandal, S.K.; Kumar, S.; Singh, P.K.; Mishra, S.K.; Bishwakarma, H.; Choudhry, N.P.; Nayak, R.K.; Das, A.K. Performance investigation of CuO-paraffin wax nanocomposite in solar water heater during night. *Thermochim. Acta* **2019**, *671*, 36–42. [CrossRef]
13. Shoeibi, S.; Kargarsharifabad, H.; Rahbar, N. Effects of nano-enhanced phase change material and nano-coated on the performance of solar stills. *J. Energy Storage* **2021**, *42*, 103061. [CrossRef]
14. Shoeibi, S.; Rahbar, N.; Abedini Esfahlani, A.; Kargarsharifabad, H. Energy matrices, economic and environmental analysis of thermoelectric solar desalination using cooling fan. *J. Therm. Anal. Calorim.* **2022**, *147*, 9645–9660. [CrossRef]
15. Demir, M.E.; Dincer, I. Development of an integrated hybrid solar thermal power system with thermoelectric generator for desalination and power production. *Desalination* **2017**, *404*, 59–71. [CrossRef]
16. Al-Waeli, A.H.A.; Sopian, K.; Kazem, H.A.; Chaichan, M.T. Evaluation of the electrical performance of a photovoltaic thermal system using nano-enhanced paraffin and nanofluids. *Case Study Therm. Eng.* **2020**, *21*, 100678. [CrossRef]
17. Olia, H.; Torabi, M.; Bahiraei, M.; Ahmadi, M.H.; Goodarzi, M.; Safaei, M.R. Application of nanofluids in thermal performance enhancement of parabolic trough solar collector: State-of-the-art. *Appl. Sci.* **2019**, *9*, 463. [CrossRef]
18. Syam Sundar, L.; Mesfin, S.; Tefera Sintie, Y.; Punnaiah, V.; Chamkha, A.J.; Sousa, A. A Review on the Use of Hybrid Nanofluid in a Solar Flat Plate and Parabolic Trough Collectors and Its Enhanced Collector Thermal Efficiency. *J. Nanofluids* **2021**, *10*, 147–171. [CrossRef]
19. Zanganeh, P.; Goharrizi, A.S.; Ayatollahi, S.; Feilizadeh, M. Nano-coated condensation surfaces enhanced the productivity of the single-slope solar still by changing the condensation mechanism. *J. Clean. Prod.* **2020**, *265*, 121758. [CrossRef]
20. Rubio, E.; Porta, M.A.; Fernández, J.L. Cavity geometry influence on mass flow rate for single and double slope solar stills. *Appl. Therm. Eng.* **2000**, *20*, 1105–1111. [CrossRef]
21. Shoeibi, S.; Kargarsharifabad, H.; Rahbar, N.; Khosravi, G.; Sharifpur, M. An integrated solar desalination with evacuated tube heat pipe solar collector and new wind ventilator external condenser. *Sustain. Energy Technol. Assess.* **2022**, *50*, 101857. [CrossRef]
22. Tohidi, F.; Ghazanfari Holagh, S.; Chitsaz, A. Thermoelectric Generators: A comprehensive review of characteristics and applications. *Appl. Therm. Eng.* **2022**, *201*, 117793. [CrossRef]
23. Lekbir, A.; Hassani, S.; Ab Ghani, M.R.; Gan, C.K.; Mekhilef, S.; Saidur, R. Improved energy conversion performance of a novel design of concentrated photovoltaic system combined with thermoelectric generator with advance cooling system. *Energy Convers. Manag.* **2018**, *177*, 19–29. [CrossRef]
24. Gu, W.; Ma, T.; Song, A.; Li, M.; Shen, L. Mathematical modelling and performance evaluation of a hybrid photovoltaic-thermoelectric system. *Energy Convers. Manag.* **2019**, *198*, 111800. [CrossRef]

25. Mohsenzadeh, M.; Shafii, M.B. A novel concentrating photovoltaic/thermal solar system combined with thermoelectric module in an integrated design. *Renew. Energy* **2017**, *113*, 822–834. [CrossRef]
26. Riahi, A.; Ali, A.B.H.; Fadhel, A.; Guizani, A.; Balghouthi, M. Performance investigation of a concentrating photovoltaic thermal hybrid solar system combined with thermoelectric generators. *Energy Convers. Manag.* **2020**, *205*, 112377. [CrossRef]
27. Yin, E.; Li, Q.; Xuan, Y. Feasibility analysis of a concentrating photovoltaic-thermoelectric-thermal cogeneration. *Appl. Energy* **2019**, *236*, 560–573. [CrossRef]
28. Li, G.; Zhao, X.; Ji, J. Conceptual development of a novel photovoltaic-thermoelectric system and preliminary economic analysis. *Energy Convers. Manag.* **2016**, *126*, 935–943. [CrossRef]
29. Li, G.; Shittu, S.; Zhao, X.; Ma, X. Preliminary experiment on a novel photovoltaic-thermoelectric system in summer. *Energy* **2019**, *188*, 116041. [CrossRef]
30. Shittu, S.; Li, G.; Zhao, X.; Zhou, J.; Ma, X.; Akhlaghi, Y.G. Experimental study and exergy analysis of photovoltaic-thermoelectric with flat plate micro-channel heat pipe. *Energy Convers. Manag.* **2020**, *207*, 112515. [CrossRef]
31. Zhu, W.; Deng, Y.; Wang, Y.; Shen, S.; Gulfam, R. High-performance photovoltaic-thermoelectric hybrid power generation system with optimized thermal management. *Energy* **2016**, *100*, 91–101. [CrossRef]
32. Shittu, S.; Li, G.; Zhao, X.; Akhlaghi, Y.G.; Ma, X.; Yu, M. Comparative study of a concentrated photovoltaic-thermoelectric system with and without flat plate heat pipe. *Energy Convers. Manag.* **2019**, *193*, 1–14. [CrossRef]
33. Bjørk, R.; Nielsen, K.K. The maximum theoretical performance of unconcentrated solar photovoltaic and thermoelectric generator systems. *Energy Convers. Manag.* **2018**, *156*, 264–268. [CrossRef]
34. Kossyvakis, D.N.; Voutsinas, G.D.; Hristoforou, E.V. Experimental analysis and performance evaluation of a tandem photovoltaic–thermoelectric hybrid system. *Energy Convers. Manag.* **2016**, *117*, 490–500. [CrossRef]
35. Rajaee, F.; Rad, M.A.V.; Kasaeian, A.; Mahian, O.; Yan, W.M. Experimental analysis of a photovoltaic/thermoelectric generator using cobalt oxide nanofluid and phase change material heat sink. *Energy Convers. Manag.* **2020**, *212*, 112780. [CrossRef]
36. Babu, C.; Ponnambalam, P. The theoretical performance evaluation of hybrid PV-TEG system. *Energy Convers. Manag.* **2018**, *173*, 450–460. [CrossRef]
37. Motiei, P.; Yaghoubi, M.; GoshtashbiRad, E.; Vadiee, A. Two-dimensional unsteady state performance analysis of a hybrid photovoltaic-thermoelectric generator. *Renew. Energy* **2018**, *119*, 551–565. [CrossRef]
38. Darkwa, J.; Calautit, J.; Du, D.; Kokogianakis, G. A numerical and experimental analysis of an integrated TEG-PCM power enhancement system for photovoltaic cells. *Appl. Energy* **2019**, *248*, 688–701. [CrossRef]
39. Roslan, Q.; Ibrahim, S.H.; Affandi, R.; Mohd Nawi, M.N.; Baharun, A. A literature review on the improvement strategies of passive design for the roofing system of the modern house in a hot and humid climate region. *Front. Archit. Res.* **2016**, *5*, 126–133. [CrossRef]
40. Khamil, K.N.; Mohd Sabri, M.F.; Md Yusop, A.; Mohd Sa'at, F.A.Z.; Isa, A.N. High cooling performances of H-shape heat sink for thermoelectric energy harvesting system (TEHs) at asphalt pavement. *Int. J. Energy Res.* **2021**, *45*, 3242–3256. [CrossRef]
41. Khamil, K.N.; Mohd Sabri, M.F.; Yusop, A.M. Thermoelectric energy harvesting system (TEHs) at asphalt pavement with a subterranean cooling method. *Energy Sources Part A Recover. Util. Environ. Eff.* **2020**, *27*, 1–17. [CrossRef]
42. Shatar, N.M.; Abdul Rahman, M.A.; Muhtazaruddin, M.N.; Shaikh Salim, S.A.Z.; Singh, B.; Muhammad Sukki, F.; Bani, N.A.; Mohd Saudi, A.S.; Ardilla Rey, J.A. Performance evaluation of unconcentrated photovoltaic-thermoelectric generator hybrid system under tropical climate. *Sustainability* **2019**, *11*, 6192. [CrossRef]
43. Ruzaimi, A.; Shafie, S.; Hassan, W.Z.W.; Azis, N.; Ya'acob, M.E.; Supeni, E.E. Photovoltaic Panel Temperature and Heat Distribution Analysis for Thermoelectric Generator Application. In Proceedings of the 2018 IEEE 5th International Conference on Smart Instrumentation, Measurement and Application (ICSIMA 2018), Songkhla, Thailand, 28–30 November 2018.
44. Sharuddin, M.S.; Yusop, A.M.; Isira, A.S.M.; Kamaruddin, N.F.; Khamil, K.N. Evaluation of voltage generation and thermal distribution from road using thermoelectric technology. *Int. J. Eng. Adv. Technol.* **2019**, *8*, 4603–4608. [CrossRef]
45. Khamil, K.N.; Sabri, M.F.M.; Yusop, A.M.; Sharuddin, M.S. An evaluation of TEC and TEG characterization for a road thermal energy harvesting. In Proceedings of the 2018 International Conference on Sustainable Energy Engineering and Application ICSEEA 2018, Tangerang, Indonesia, 1–2 November 2018.
46. Wan Jamaludin, W.A.; Johar, M.A.; Faizan Marwah, O.M.; Amin, A.M. Evaluation of the potential of renewable thermal energy from shingles using thermoelectric generator (TEG) for residential use application. *J. Adv. Res. Fluid Mech. Therm. Sci.* **2020**, *70*, 50–58. [CrossRef]
47. Baharin, N.A.; Arzami, A.A.; Singh, B.; Remeli, M.F.; Tan, L.; Oberoi, A. Passive flow heat exchanger simulation for power generation from solar pond using thermoelectric generators. *AIP Conf. Proceed.* **2017**, *2017*, 020021.
48. Daud, M.M.M.; Nor, N.B.M.; Ibrahim, T. Novel hybrid photovoltaic and thermoelectric panel. In Proceedings of the 2012 IEEE International Power Engineering and Optimization Conference, Melaka, Malaysia, 6–7 June 2012.
49. Wai, N.; Ahmad, S.; Hagishima, A.; Bahadur, H.; Yakub, F. Energy & Buildings Affordable retrofitting methods to achieve thermal comfort for a terrace house in Malaysia with a hot—humid climate. *Energy Build.* **2020**, *223*, 110072.
50. Al-Obaidi, K.M.; Ismail, M.; Rahman, A.M.A. Passive cooling techniques through reflective and radiative roofs in tropical houses in Southeast Asia: A literature review. *Front. Archit. Res.* **2014**, *3*, 283–297. [CrossRef]
51. Lee, Y.Y.; Md Din, M.F.; Iwao, K.; Lee, Y.H.; Anting, N. Impact of thermal behaviour of different environmental conditions on ambient environment and thermal discomfort in Malaysia. *Indoor Built Environ.* **2020**, *30*, 520–534. [CrossRef]

52. Hafeez, M.; Nasir, A.; Hassan, A.S. Thermal performance of double brick wall construction on the building envelope of high-rise hotel in Malaysia. *J. Build. Eng.* **2020**, *31*, 101389.
53. Toe, D.H.C.; Kubota, T. Comparative assessment of vernacular passive cooling techniques for improving indoor thermal comfort of modern terraced houses in hot–humid climate of Malaysia. *Sol. Energy* **2015**, *114*, 229–258. [CrossRef]
54. Dillersberger, H.; Deutschmann, B.; Tham, D. A bipolar ±13 mV self-starting and 85% peak efficiency DC/DC converter for thermoelectric energy harvesting. *Energies* **2020**, *13*, 5501. [CrossRef]
55. Zhao, D.; Aili, A.; Yin, X.; Tan, G.; Yang, R. Roof-integrated radiative air-cooling system to achieve cooler attic for building energy saving. *Energy Build.* **2019**, *203*, 109453. [CrossRef]
56. Ismail, M.I.; Yunus, N.A.; Hashim, H. The challenges and opportunities of solar thermal for palm oil industry in Malaysia. *Chem. Eng. Trans.* **2020**, *78*, 601–606.
57. Wu, Z.; Zhang, S.; Liu, Z.; Mu, E.; Hu, Z. Thermoelectric converter: Strategies from materials to device application. *Nano Energy* **2022**, *91*, 106692. [CrossRef]
58. Cao, P.; Hong, Z. A Bipolar-Input Bipolar-Output DC-DC Converter for Thermoelectric Energy Harvesting. In Proceedings of the 2019 IEEE International Symposium on Circuit and Systems (ISCAS), Hokkaido, Japan, 26–29 May 2019.
59. Lineykin, S.; Sitbon, M.; Kuperman, A. Design and optimization of low-temperature gradient thermoelectric harvester for wireless sensor network node on water pipelines. *Appl. Energy* **2021**, *283*, 116240. [CrossRef]
60. Kuai, Q.; Wan, Q.; Mok, P.K.T. An auto-polarity thermoelectric energy harvesting interface based on a boost/buck-boost converter. In Proceedings of the 2019 IEEE International Symposium on Circuit and Systems (ISCAS), Hokkaido, Japan, 26–29 May 2019.
61. Cao, P.; Qian, Y.; Xue, P.; Lu, D.; He, J.; Hong, Z. 27.1 An 84% Peak Efficiency Bipolar-Input Boost/Flyback Hybrid Converter with MPPT and on-Chip Cold Starter for Thermoelectric Energy Harvesting. In Proceedings of the 2019 IEEE International Solid-State Circuits Conference–(ISSCC), San Francisco, CA, USA, 17–21 February 2019.
62. Cao, P.; Qian, Y.; Xue, P.; Lu, D.; He, J.; Hong, Z. A Bipolar-Input Thermoelectric Energy-Harvesting Interface with Boost/Flyback Hybrid Converter and On-Chip Cold Starter. *IEEE J. Solid-State Circuits* **2019**, *54*, 3362–3374. [CrossRef]
63. Nozariasbmarz, A.; Collins, H.; Dsauza, K.; Polash, M.H.; Hosseini, M.; Hyland, M.; Liu, J.; Malhotra, A.; Ortiz, F.M.; Mohaddes, F.; et al. Review of wearable thermoelectric energy harvesting: From body temperature to electronic systems. *Appl. Energy* **2019**, *258*, 114069. [CrossRef]
64. Rejab, M.N.; Johar, M.A. Evaluation of thermoelectric generator array configuration for thermal energy harvesting at the rooftop and attic area due to solar radiation in Malaysia. In Proceedings of the 2022 International Electrical Engineering Congress (iEECON), Khon Kaen, Thailand, 9–11 March 2022.
65. Rejab, M.N.; Johar, M.A. A comprehensive data analysis method focuses on complex real-time temperature data of thermoelectric generator. In Proceedings of the 10th European Conference of Renewable Energy System (ECRES), Istanbul, Turkey, 7–9 May 2022.
66. Islam, H.; Mekhilef, S.; Shah, N.B.M.; Soon, T.K.; Seyedmahmousian, M.; Horan, B.; Stojcevski, A. Performance evaluation of maximum power point tracking approaches and photovoltaic systems. *Energies* **2018**, *11*, 365. [CrossRef]
67. Mamur, H.; Üstüner, M.A.; Bhuiyan, M.R.A. Future perspective and current situation of maximum power point tracking methods in thermoelectric generators. *Sustain. Energy Technol. Assess.* **2022**, *50*, 101824. [CrossRef]
68. Amjad, M.; Farooq-i-azam, M.; Ni, Q.; Dong, M.; Ahmad, E. Wireless charging systems for electric vehicles. *Renew. Sustain. Energy Rev.* **2022**, *167*, 112730. [CrossRef]
69. Dalala, Z.M.; Saadeh, O.; Bdour, M.; Zahid, Z.U. A new maximum power point tracking (MPPT) algorithm for thermoelectric generators with reduced voltage sensors count control. *Energies* **2018**, *11*, 1826. [CrossRef]
70. Lin, Y.; Wu, T.; Zeng, Y.; Yang, J.; Chen, W.; Li, Z. A 15 mV-input and 71%-efficiency boost converter with 22 mV output ripple for thermoelectric energy harvesting application. *Microelectron. J.* **2022**, *121*, 105353. [CrossRef]
71. Wang, K.; Guan, M.; Chen, F.; Liao, W.H. A Low-Power Thermoelectric Energy Harvesting System for High Internal Resistance Thermoelectric Generators. *J. Electron. Mater.* **2019**, *48*, 5375–5389. [CrossRef]
72. Kimura, K.; Koizumi, H. A bipolar power converter with bridgeless boost rectifier for thermoelectric energy harvesting. In Proceedings of the 2015 IEEE 2nd International Future Energy Electronic Conference (IFEEC), Taipei, Taiwan, 1–4 November 2015.
73. Taeda, K.; Koizumi, H. A bipolar self-start up boost converter for thermoelectric energy harvesting. In Proceedings of the 2017 IEEE Energy Conversion Congress and Exposition (ECCE), Cincinnati, OH, USA, 1–5 October 2017.
74. Taeda, K.; Shiina, N.; Kimura, K.; Koizumi, H. A thermoelectric energy harvesting system with bridgeless boost/buck-boost rectifier. In Proceedings of the IECON 2017—43rd Annual Conference of the IEEE Industrial Electronic Society, Beijing, China, 29 October–1 November 2017.
75. Kimura, K.; Taeda, K.; Niikawa, S.; Koizumi, H. A Wireless Sensor Node Driving System with Bridgeless Bipolar Boost Rectifier Using Thermoelectric Energy Harvesting. In Proceedings of the 2018 IEEE International Symposium on Circuits and System, Florence, Italy, 27–30 May 2018.
76. Sigrist, L.; Stricker, N.; Bernath, D.; Beutel, J.; Thiele, L. Thermoelectric Energy Harvesting from Gradients in the Earth Surface. *IEEE Transit. Ind. Electron.* **2020**, *67*, 9460–9470. [CrossRef]
77. Siddique, A.R.M.; Mahmud, S.; Van Heyst, B. A review of the state of the science on wearable thermoelectric power generators (TEGs) and their existing challenges. *Renew. Sustain. Energy Rev.* **2017**, *73*, 730–744. [CrossRef]
78. Pappinisseri Puluckul, P.; Weyn, M. Battery-Less Environment Sensor Using Thermoelectric Energy Harvesting from Soil-Ambient Air Temperature Differences. *Sensors* **2022**, *22*, 4737. [CrossRef]